catalysts

MDPI

Article

Atmospheric-Pressure Microplasma Synthesis of Palladium Nanoparticles for Environmental Catalysis

Siddiqa Ismail [1], Waqqar Ahmed [2], Akif Naqeeb Qadri [1], Niaz Wali [3], Najeeb Ur Rehman [1,*], Yakup Yildirim [4,5] and Taha Radwan [6,*]

[1] Plasma Physics Laboratory, Department of Physics, COMSATS University Islamabad, Islamabad 45550, Pakistan
[2] Materials Laboratory, Department of Physics, COMSATS University Islamabad, Islamabad 45550, Pakistan
[3] Department of Physics, Qilu Institute of Technology, Jinan 250200, China
[4] Department of Computer Engineering, Biruni University, Istanbul 34010, Turkey
[5] Mathematics Research Center, Near East University, Nicosia 99138, Cyprus
[6] Department of Management Information Systems, College of Business and Economics, Qassim University, Buraydah 51452, Saudi Arabia
* Correspondence: najeeb-ur-rehman@comsats.edu.pk (N.U.R.); t.radwan@qu.edu.sa (T.R.)

Abstract

Atmospheric-pressure plasma–liquid interactions (PLIs) enable nanoparticle synthesis by generating reactive reducing species directly at the plasma–liquid interface, without the addition of a separate chemical reductant. In this work, d-fructose-stabilized palladium nanoparticles (Pd NPs) were synthesized in a one-step atmospheric-pressure DC microplasma process using chloropalladic acid as the precursor. Optical emission spectroscopy was used to examine plasma characteristics governing nanoparticle formation. The discharge produced OH radicals, UV radiation, and excited argon species, while electron and gas temperatures were evaluated with discharge current. Increasing current enhanced UV emission, relative OH emission intensity, and gas temperature, whereas electron temperature decreased because of greater collisional energy transfer. These plasma-driven processes promoted Pd^{2+} reduction and influenced nanoparticle nucleation and growth. UV–Vis spectroscopy showed progressive conversion of Pd^{2+} to metallic Pd, with most growth completed within 30 min. SEM and EDX confirmed predominantly spherical, d-fructose-stabilized metallic Pd nanostructures, while XRD further supported the formation of crystalline metallic Pd^0 with an fcc structure. The Pd NPs showed strong catalytic activity for reducing 4-nitrophenol, methyl orange, and Congo red, with apparent rate constants of 0.2508, 0.6346, and 0.3416 min^{-1}, respectively. These findings demonstrate atmospheric-pressure PLI as a controllable platform for producing catalytically active palladium nanoparticles in an aqueous medium.

Keywords: plasma–liquid interactions; optimization; palladium nanoparticles; d-fructose stabilization; plasma-assisted synthesis; catalytic degradation

Check for updates

Academic Editors: Khursheed B. Ansari and Shakeelur Raheman Ateequr Raheman

Received: 7 September 2026
Revised: 7 October 2026
Accepted: 13 October 2026
Published: 15 October 2026

Copyright: © 2026 by the authors. Licensee MDPI, Basel, Switzerland. This article is an open access article distributed under the terms and conditions of the Creative Commons Attribution (CC BY) license.

1. Introduction

Metal nanoparticles (NPs) have received significant attention in recent years due to their optical, electrical, magnetic, and electronic properties [1–4]. Owing to these properties, metal NPs have been employed in various applications, such as biosensing, photo-thermal therapy, drug delivery, electrical sensing, etc. [5–8]. Among noble metals, palladium nanoparticles (Pd NPs) in particular exhibit characteristics such as high selectivity, adsorption, and stability [9,10]. As a result, Pd NPs have obtained significant importance

in applications such as catalysis, hydrogen storage, heavy metal reduction, and organic synthesis [11,12]. In addition, Pd NPs have shown high efficiency in coupling and hydrogenation reactions [13,14].

The urgent need to address water pollution from industrial dyes provides a compelling application for such nanocatalysts. The catalytic reduction and degradation of organic dyes have also been achieved using Pd NPs. The discharge of synthetic dye effluents from textile, leather, paper, and plastic manufacturing constitutes a major environmental challenge [15–17]. Most of these dyes include azo structures, which are highly toxic, mutagenic, and carcinogenic in nature [18]. The inhalation or ingestion of such molecules can cause severe health hazards, and their release into water bodies also poses a danger to aquatic and marine life. Moreover, due to their low biodegradability, these molecules are less prone to decomposition, which necessitates their removal from the environment using physical or chemical methods [19]. Therefore, the application of nanocatalysts such as Pd NPs for the catalytic reduction and transformation of dyes, with the potential for subsequent treatment of the resulting products, holds considerable significance for wastewater treatment.

The physical characteristics of Pd NPs, such as size, shape, and dispersity, influence their catalytic activity. Accordingly, there has been substantial progress in the synthesis of Pd NPs using various methods. The most common method for the synthesis of Pd NPs is the chemical method, which involves the use of reducing agents such as sodium borohydride, ascorbic acid, dimethyl formamide, hydrazine, carboxylic acid, etc. [20–24]. It also requires the use of stabilizing agents such as cetyltrimethylammonium bromide (CTAB), sodium citrate, etc., in order to control the growth of the NPs [25,26]. Other methods for the synthesis of Pd NPs include hydrothermal, sono-chemical, physical vapor deposition (PVD), laser ablation, and biogenic synthesis [27–31]. Many of these techniques are multistep procedures that involve the use of toxic compounds as reducing and stabilizing agents, reducing the biocompatibility of the NPs and resulting in the formation of toxic byproducts. Additionally, the requirement of conditions, such as high temperatures or pressure, poor yield, and minimal control over the growth of NPs, are also significant drawbacks of these processes.

Plasma technology has emerged as an effective approach to nanoparticle synthesis. Cold plasma operating at both atmospheric and low pressure has been employed by many researchers for the synthesis of metal NPs. The synthesis process involves a plasma–liquid interaction (PLI) technique in which cold plasma comes into contact with the aqueous medium containing salt precursors [32,33]. The interaction of plasma with liquid results in processes such as ionization, sputtering, excitation, evaporation, and dissociation. Moreover, a series of electrochemical reactions are initiated at the plasma–liquid interface, due to which a diverse range of reducing species are formed automatically in PLIs [34]. Therefore, in contrast to conventional methods, PLI is a reagent-minimized and facile technique in which the synthesis of NPs can be achieved without the addition of external reducing agents. The growth of NPs can also be controlled by varying parameters such as discharge current, flow rates, precursor concentration, reaction time, etc.

Several researchers have utilized plasma for the synthesis of metal NPs, such as Au, Ag, Pt, Pd, etc. The synthesis of NPs has been performed by generating plasma using a variety of discharge sources and working gases under different conditions. Wang et al. reported the synthesis of gold and palladium nanoparticles (AuNPs and Pd NPs) with a branched structure by using a glow discharge plasma at low pressure [35]. Similarly, Pd NPs supported on carbon were synthesized by Liu et al. using low-pressure argon plasma for their application in Suzuki and Heck coupling reactions [36]. However, the low-pressure operation of plasma in these systems can be costly, which limits their industrial

application. Hence, synthesis of Pd NPs has also been attempted at atmospheric pressure by various research groups. Zhao et al. employed atmospheric-pressure plasma generated using an AC voltage source for the fabrication of Pd catalysts supported by graphene. The synthesis was performed using both atmospheric and thermal H_2 plasma, and the results were compared [37]. The reduction of Pd and other metal ions supported on TiO_2 was performed by Di et al. using CO atmospheric pressure plasma. In the study, the reduction of ions into metal NPs was also compared for CO and H_2 plasma [38]. Despite significant progress in the plasma-assisted synthesis of Pd NPs, most reported studies focus on supported catalysts or rely on low-pressure or complex atmospheric plasma systems [39,40]. Moreover, the synthesis of stable colloidal Pd NPs at atmospheric pressure using simple DC PLI configurations remains relatively unexplored. In addition, only limited attention has been given to the role of plasma-generated reactive species and UV radiation in governing NP formation under such conditions. The present work addresses these gaps by demonstrating a straightforward atmospheric PLI approach for the synthesis of biocompatible, d-fructose-stabilized colloidal Pd NPs while systematically correlating discharge parameters with plasma characteristics and NP formation behavior.

In this research, the synthesis of colloidal Pd NPs at atmospheric pressure has been reported by employing the PLI technique. A DC discharge plasma is generated over an aqueous palladium precursor solution, and d-fructose is used as a surfactant to stabilize the NPs. The influence of discharge parameters on plasma characteristics and NP formation is investigated. Furthermore, the catalytic activity of the synthesized Pd NPs has been evaluated for the degradation of toxic dye molecules.

2. Experimental Results and Discussion

The present study reports the synthesis of colloidal Pd NPs using a plasma–liquid interaction (PLI) technique. Atmospheric pressure microplasma transports a variety of reactive species to the precursor solution. These reactive species include highly energetic electrons, reactive oxygen and nitrogen species (RNOS), OH radicals, etc. [41,42]. As the transfer of such species occurs from the plasma to the liquid electrolyte, chemical reactions that are pertinent to the synthesis of NPs take place at the interface [43]. Consequently, the nucleation of NPs is initiated, and the synthesis of d-fructose-coated Pd NPs is achieved through the reduction of metal ions. Therefore, to understand the synthesis of Pd NPs, the production of reactive species in plasma is evaluated through optical emission spectroscopy (OES), and the synthesized NPs are then studied using different characterization techniques.

2.1. Plasma Diagnostics via OES

Plasma-assisted synthesis relies on the precise control of different plasma parameters and the production of reactive species that play an important role in driving the desired chemical and physical reactions at the plasma–liquid interface. Hence, the present study focuses on varying the discharge current to investigate its effect on the generation of UV radiation and hydroxyl (OH) radicals. Additionally, the effect of discharge current on key plasma parameters, such as electron temperature (T_e) and gas temperature (T_g), has been analyzed.

The time-integrated optical emission spectrum obtained from argon plasma discharge measured at a discharge current of 5 mA and a gas flow rate of 100 SCCM is shown in Figure 1. The spectrum consists of several peaks corresponding to various reactive species in the plasma. The peak at 309 nm indicates the presence of OH radicals, which are formed due to the dissociation of water molecules as a result of electron impact near the interface [44]. The peaks at 337 nm and 381 nm are associated with the second positive system of nitrogen ($C^3\Pi_u \rightarrow B^3\Pi_g$), which is detected when air mixes with plasma [45].

The most intense peaks are observed in the range of 696 nm to 826 nm, corresponding to well-known argon atomic lines related to transitions between electron energy levels in the argon atom. These emission lines confirm the generation of argon plasma along with reactive molecular species.

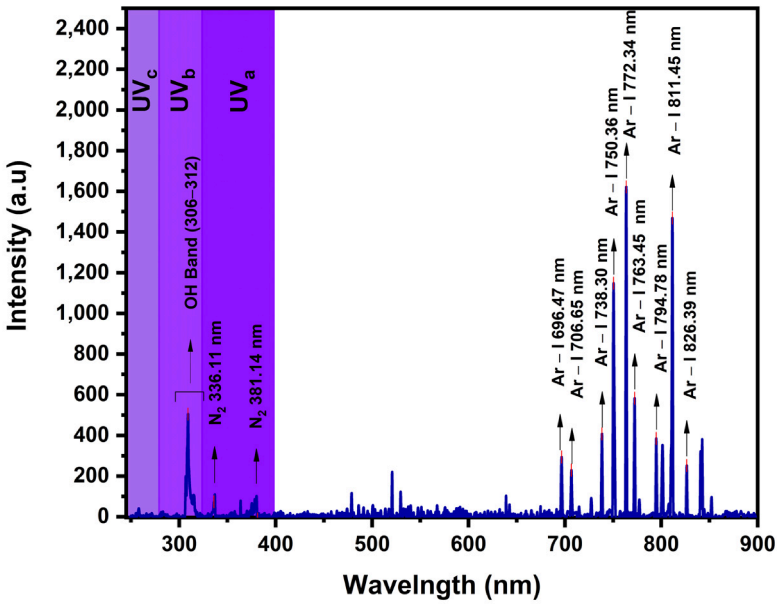


Figure 1. OES spectrum of Ar plasma discharge at a 5 mA current.

The OES spectrum also reveals the production of UV radiation, which acts as a reducing agent and triggers multiple chemical reactions. The UV radiation consists of three major categories, i.e., UV_a (320–400 nm), UV_b (280–320 nm), and UV_c (250–280 nm) radiation. UV_a is the least energetic among these radiations; however, it penetrates deeper into the liquid, causing indirect reactions and the formation of radicals. UV_b has intermediate photon energy and promotes photochemical reactions by breaking chemical bonds. UV_c has the highest energy and is able to directly dissociate and ionize molecules, which contributes to the formation of ions and OH radicals that are essential for nanoparticle synthesis [46,47]. The effect of discharge current on UV radiation intensity was studied by recording the emission spectra as the discharge current varied from 5 mA to 7 mA. It was noted that the intensities of UV_a, UV_b, and UV_c radiation increased with the rise in discharge current, as shown in Figure 2a.

The enhancement in UV radiation intensity can be attributed to the higher electron density at elevated current values, which increases excitation and emission processes in the plasma. Figure 2b shows the variation in relative OH emission intensity with the discharge current. Raising the discharge current leads to frequent collisions between energetic electrons and water molecules, thereby elevating the concentration of OH radicals [48]. Furthermore, the increase in UV radiation intensity with the discharge current also causes UV-induced water photolysis, which enhances OH radical density. Thus, the increase in discharge current results in increases in UV_a, UV_b, and UV_c radiation, along with OH emission intensity [49]. However, it is noted that excessive UV intensity and radical concentration may lead to rapid nucleation and the uncontrolled growth of nanoparticles. Moreover, a high current can generate disproportionate thermal and chemical energy, disrupting the required nucleation–growth balance for nanoparticle synthesis.

The electron temperature T_e and gas temperature T_g were determined using optical emission spectroscopy (OES) to analyze the microplasma during NP synthesis. As argon

was used as a working gas, T_e was calculated using the Boltzmann plot method from Ar I emission lines, and the following equation was used (Figure 3).

$$\ln\left(\frac{I_{ki}\lambda_{ki}}{g_k A_{ki}}\right) = -\frac{E_k}{K_B T_e} + C$$

where A_{ki} represents the transition probability, g_k is the statistical weight of the upper level, E_k is the excited state energy level, K_B is the Boltzmann constant, λ_{ki} is the transition wavelength, and I_{ki} denotes the measured emission intensity [50]. The slope of the plot of $\ln(I_{ki}\lambda_{ki}/g_k A_{ki})$ vs. E_k is used to obtain the electron temperature.

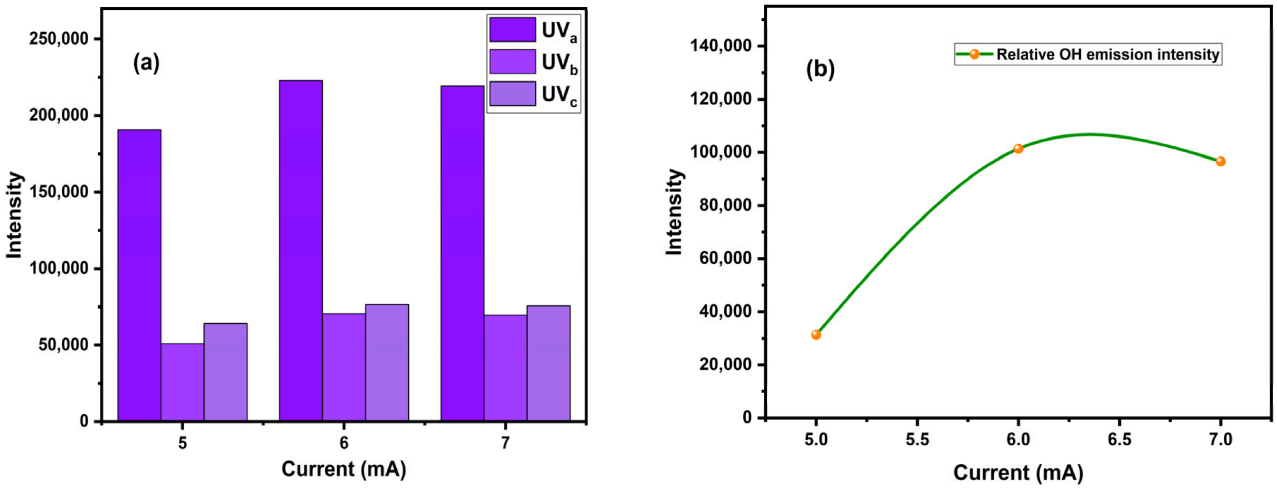


Figure 2. Variation in (**a**) UV radiation intensity and (**b**) relative OH emission intensity with discharge current.

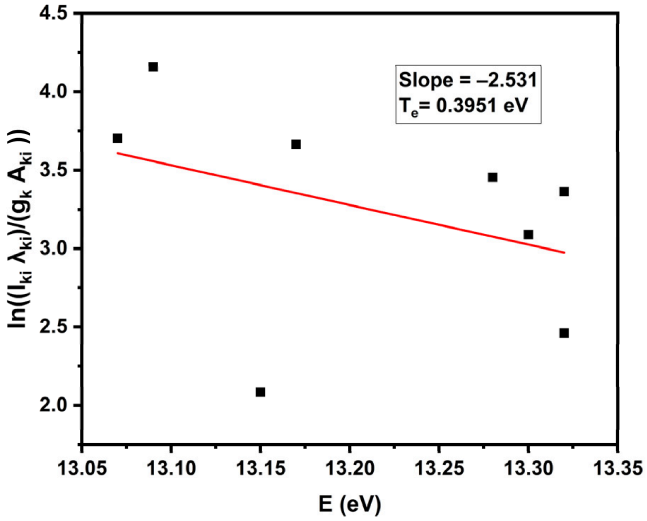


Figure 3. Boltzmann plot for the determination of electron temperature at a discharge current of 7 mA.

It was found that T_e decreased as the discharge current was increased from 5 mA to 7 mA (Figure 4a). The decreasing trend in T_e is linked to the enhanced number density at higher discharge currents, which causes increased collisions between electrons and neutral species in the plasma. These collisions result in the dissipation of energy through processes such as ionization, excitation, etc. Therefore, the average electron energy, represented by the electron temperature T_e, is reduced [51].

The gas temperature T_g was obtained using the Boltzmann plot method based on rotational transitions of the OH band (306–312 nm) [52,53]. The Q1 branch lines of the OH

band ($A^2\Sigma^+ - X^2\Pi$) transitions were used. The OH branch lines Q1 and R1 in the emission spectra have been labeled in Figure 4b, in which only Q1 lines have been selected for the estimation of the rotational temperature. Their emission intensities follow the relation given as:

$$I_{jj'} \propto h\nu_{jj'}(2J+1)A_{jj'}\exp\left(-\frac{B_v hcJ(J+1)}{K_B T_{rot}}\right)$$

where $I_{jj'}$ is the measured intensity of the rotational transition, $\nu_{jj'}$ is the transition frequency, (2J + 1) is the rotational degeneracy of the upper rotational level, and the term $B_\upsilon J(J+1)$ represents the rotational energy of the selected rotational level, which is expressed in E(cm^{-1}) [54]. Figure 4c shows the Boltzmann plot constructed using the selected emission lines and their corresponding energies. The rotational temperature T_{rot} was determined from the slope of the plot between $\ln(I/(2J+1)A_{jj'})$ and E(cm^{-1}). Under atmospheric plasma conditions, the rotational temperature estimated from the OH band is assumed to be a reliable approximation of T_g. Using this approach, T_g was found to increase as the discharge current was raised from 5 mA to 7 mA (Figure 4d), indicating an increase in the energy transfer to molecular species [55]. At higher values of the discharge current, the collisions between the electrons and neutral species in the plasma are more frequent, due to which energy transfer occurs, causing the heating of the neutral gas. This results in the enhancement of the kinetic energy of gas molecules, leading to a rise in the gas temperature.

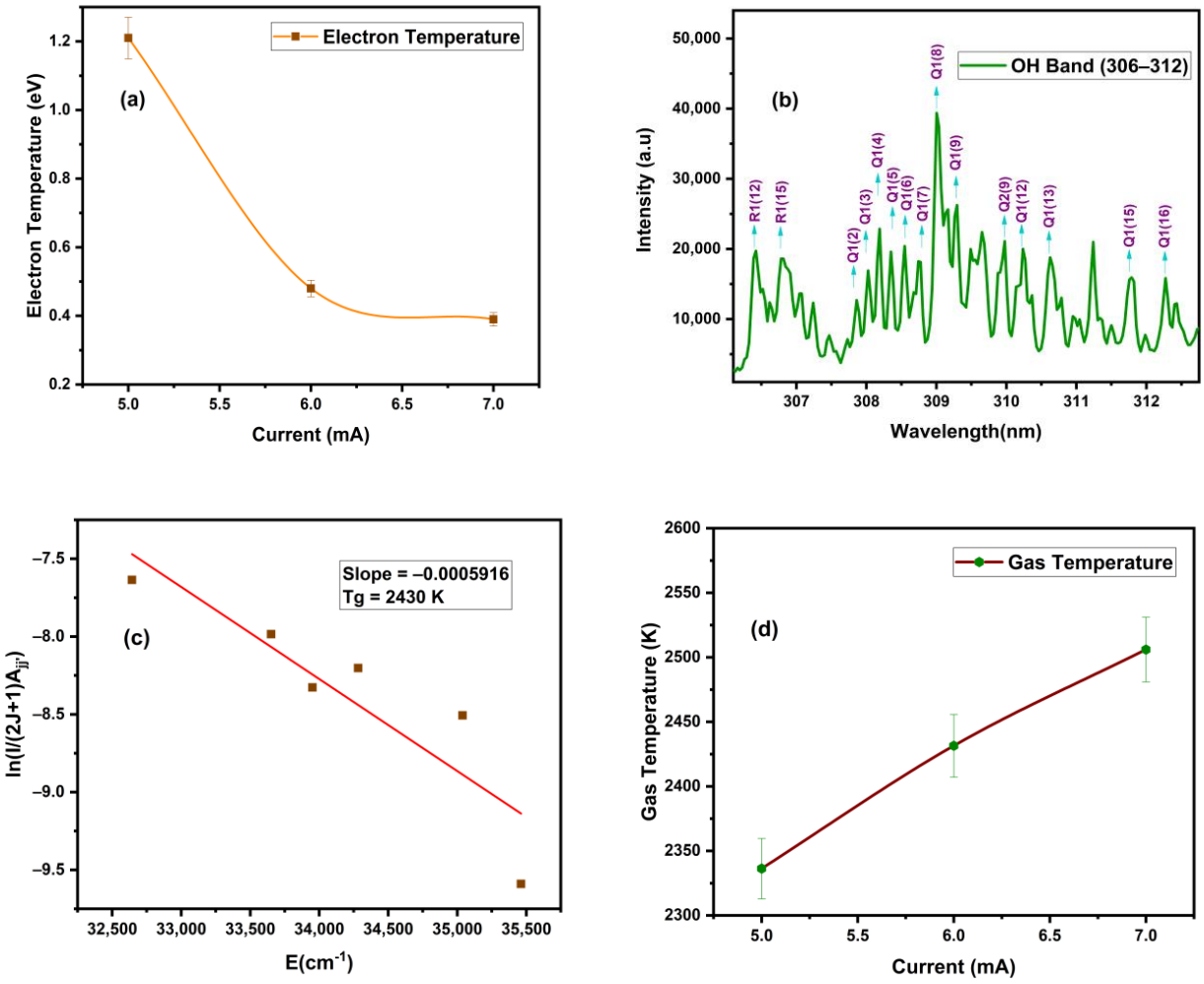


Figure 4. (**a**) Variation in T_e with discharge current. (**b**) OH transition band. (**c**) Boltzmann plot for the estimation of T_g at a 6 mA discharge current and a 100 SCCM gas flow rate. (**d**) Variation in T_g with an increase in the discharge current.

In addition to OES, the OH concentration in the liquid phase was quantitatively estimated using the terephthalic acid (TA) chemical dosimetry method reported by Farooq et al. [56]. OH radicals react with TA to form 2-hydroxyterephthalic acid (HTA), whose fluorescence was measured at 425 nm following excitation at 310 nm. A calibration curve obtained using known HTA concentrations was used to determine the corresponding OH concentration. The measured OH concentrations are reported in millimoles (mM), based on the 20 mL volume of the treated solution, and are represented in Figure 5a,b. The results show an increase in the cumulative OH concentration with increasing plasma treatment time, supporting the role of plasma-generated OH in the liquid-phase chemistry involved in Pd NP formation. Although the concentration of OH increased with plasma treatment time, OH radicals are highly reactive, short-lived radicals and should not be directly equated with bulk alkalinity. With prolonged plasma exposure, the accumulation of reactive nitrogen species and their conversion to nitrite/nitrate can contribute to the acidification of plasma-treated water.

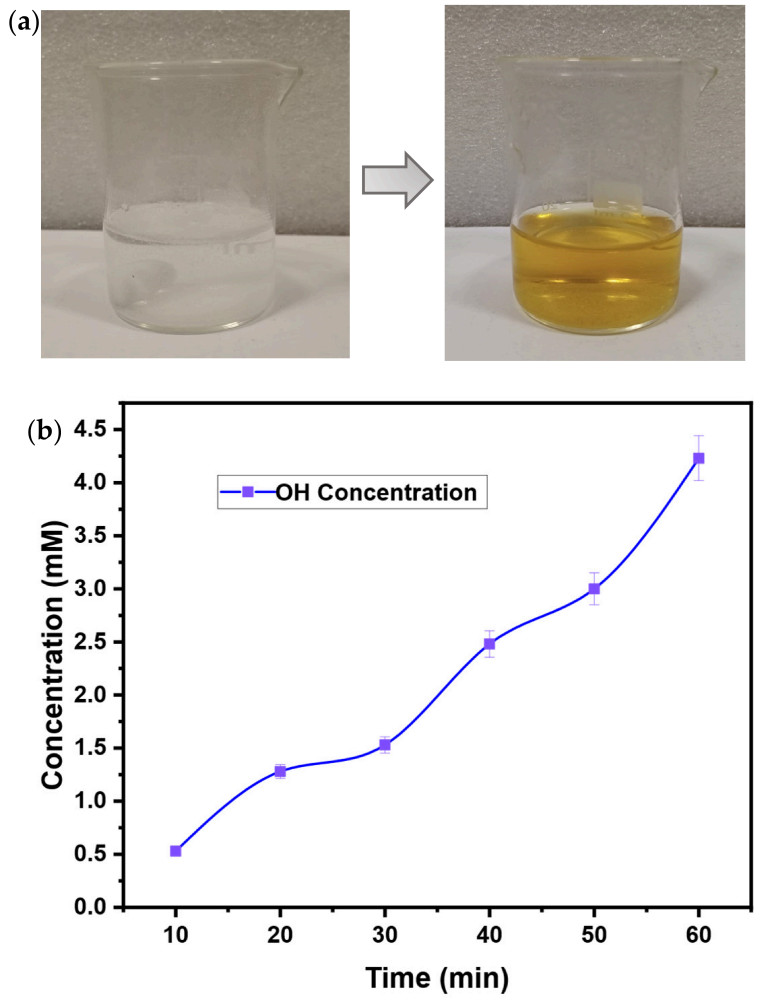


Figure 5. (**a**) Formation of 2-HTA from TA after plasma treatment. (**b**) Estimated OH concentration as a function of plasma treatment time.

The variations in T_e, T_g, and the generation of reactive species, i.e., UV radiation and OH radicals, are significant parameters influencing the growth of NPs. While T_e decreases with the discharge current, higher T_e values are crucial for the formation of reactive species and the reduction of Pd ions. In contrast, T_g, UV intensity, and relative OH emission intensity increase with the discharge current, enhancing the thermal and chemical activity within the system. Although reactive species are essential for the reduction of ions,

their excessive production combined with high T_g can lead to uncontrolled nucleation and particle agglomeration. To ensure uniform Pd NP synthesis, a discharge current of 5 mA was selected during the synthesis to maintain a balanced and controlled reactive environment.

The electrical characteristics of the discharge were monitored using a high-voltage probe and oscilloscope while varying the discharge current from 5 to 7 mA (Figure 6a,b). The RMS current and voltage measured were 4.90 mA/7.760 kV, 5.61 mA/7.780 kV, and 6.62 mA/7.823 kV for the 5, 6, and 7 mA operating conditions, respectively. The effective electrical power was estimated using $P_{eff} = V_{rms}\, I_{rms}$, yielding approximately 38.02, 43.65, and 51.79 W, respectively.

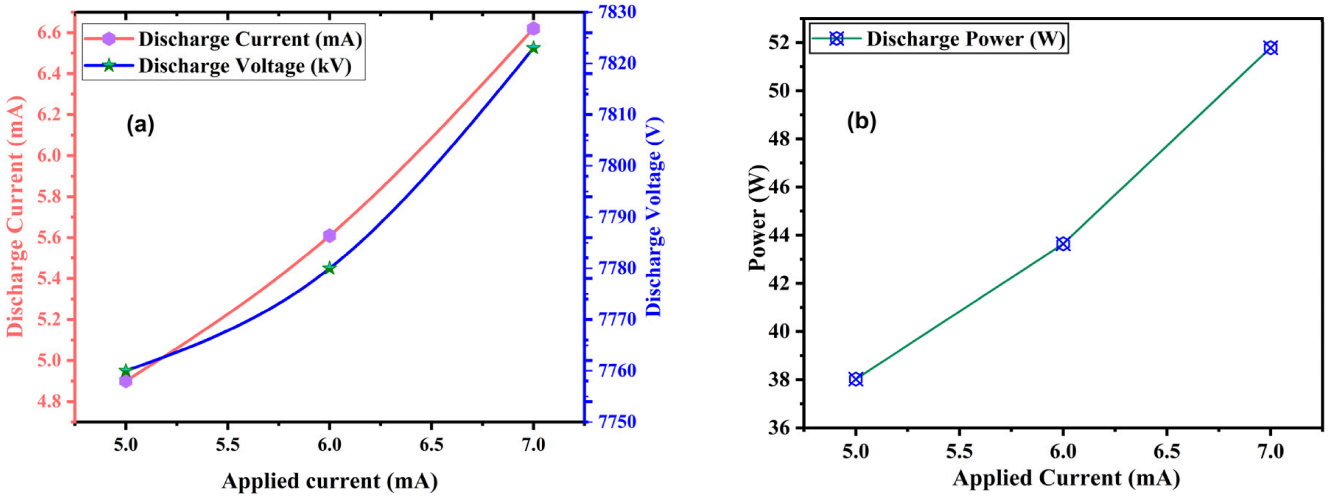


Figure 6. Electrical characteristics of the DC discharge in the plasma–liquid interaction: (**a**) measured discharge current and voltage as a function of applied current; (**b**) discharge power at different applied currents.

2.2. Synthesis and Characterization of Pd NPs

To synthesize Pd NPs, chloropalladic acid H_2PdCl_4 and d-fructose were added to deionized (DI) water in a glass beaker, and the solution mixture was placed under an atmospheric-pressure microplasma. Two samples of Pd NPs were prepared by dissolving the H_2PdCl_4 and d-fructose (0.1 M) solution in different concentrations. The molar concentration of H_2PdCl_4 was varied from 0.4 mM to 0.6 mM as 4 mL and 6 mL of H_2PdCl_4 (2 mM) were added to DI water, making the total volume 20 mL in each case. Furthermore, the d-fructose concentration varied from 4 mM to 6 mM in the respective samples. As a result, samples S1 (0.4/4 mM H_2PdCl_4/d-fructose) and S2 (0.6/6 mM H_2PdCl_4/d-fructose) were synthesized using the PLI technique. Before plasma treatment, the initial pH and temperature of the precursor solution were 2.75 and 24.4 °C, respectively. During plasma treatment, the pH changed to 6.20, 4.80, and 2.60 after 10, 20, and 30 min, while the temperature increased to 31.7, 35.4, and 42.3 °C, respectively. The initial increase in pH followed by acidification indicates that the plasma–liquid interaction involves competing chemical processes rather than a monotonic change in acidity. Plasma treatment generates short-lived reactive species, including OH, which rapidly undergo secondary reactions and contribute to the formation of longer-lived reactive oxygen and nitrogen species [1]. With prolonged treatment, the accumulation of species, such as nitrite, nitrate, and hydrogen peroxide, can promote acidification of the liquid.

The progressive increase in the bulk-liquid temperature can be attributed to energy transfer from the plasma discharge to the liquid. Plasma–liquid interactions involve coupled heat and mass transfer processes at the plasma–liquid interface, and continuous plasma exposure can consequently lead to heating of the treated liquid. In particular,

energy transfer associated with the plasma species and interfacial processes, together with electrical and thermal energy dissipation in the discharge–liquid system, contributes to the observed temperature increase [57,58]. After synthesis, samples were centrifuged at 10,000 rpm for 10 min and re-dispersed in deionized (DI) water to reduce soluble species associated with the recovered nanoparticles. This separation transfers soluble species to the supernatant rather than eliminating them from the overall process. Residual dissolved palladium and chloride were not quantified; therefore, complete removal of these species is not claimed. The collected nanoparticles were subsequently used for characterization.

UV–Vis spectroscopy was employed to evaluate the formation of Pd NPs. To monitor the synthesis, the UV–Vis spectra of Pd NPs were taken every 10 min during the synthesis process (shown in Figure 7a,b). The absorption spectra of the H_2PdCl_4 solution before plasma treatment showed weak absorption in the ultraviolet and visible region. However, with the increase in time, the intensity of absorption increased in the UV region, as a shoulder and peak at 278 nm and 388 nm were observed. It can be suggested that the presence of these peaks is attributed to the increase in Pd^{2+} ions in the solution. With further increases in time, the peaks began to disappear as the absorbance of the solution increased further. This indicated the conversion of Pd^{2+} ions into Pd^0, causing the nucleation and growth of Pd NPs [59]. It can be concluded that most of the Pd NP growth was completed within 30 min of plasma treatment, as minimal change in the absorbance was observed afterwards. The color of the solution mixture also varied during the synthesis of Pd NPs. Before plasma treatment, the color of the electrolyte solution was light yellow. However, as the synthesis process progressed, the solution turned light gray and finally became dark gray, indicating the synthesis of Pd NPs.

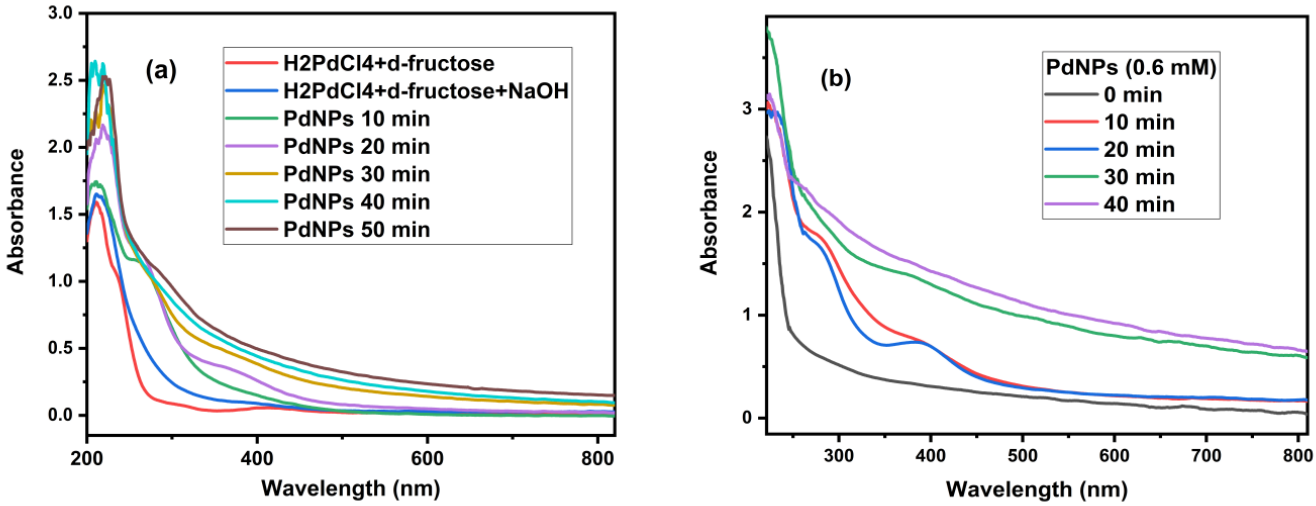


Figure 7. UV–Vis spectra of Pd NP samples (**a**) S1 (0.4 mM) and (**b**) S2 (0.6 mM).

The size and morphology of the synthesized Pd NPs were investigated using SEM. Figure 8a,b show the SEM images of Pd NPs synthesized using different precursor concentrations, i.e., 0.4 mM (S1) and 0.6 mM (S2) H_2PdCl_4, respectively. The S1 sample shows predominantly individual, approximately spherical nanoparticles with relatively limited aggregation. The average particle size and corresponding particle-size distribution of S1 are presented in Figure 8c. In contrast, the S2 sample showed Pd NPs having larger particle sizes and exhibited a higher degree of aggregation, with nanoparticles forming clustered and interconnected structures. The increase in particle size is consistent with previous reports of NP synthesis using the PLI technique, in which a higher precursor concentration resulted in larger particle sizes [60]. However, in this case, an increase in precursor concentration also led to the formation of larger clusters due to the aggregation

of Pd NPs. The cluster formation occurs on SEM substrates during the drying process and can be attributed to capillary forces that induce interactions between NPs, resulting in aggregation.

EDX analysis of the synthesized Pd NPs (S1 sample) was performed, and the elemental analysis of the NPs is depicted in Figure 8d. The peak at 2.8 keV corresponds to Pd, indicating that Pd is present in its metallic form in the sample, whereas the peak at 1.8 keV in the spectrum is the Si peak, which is associated with the Si substrate on which Pd NPs were deposited for the analysis.

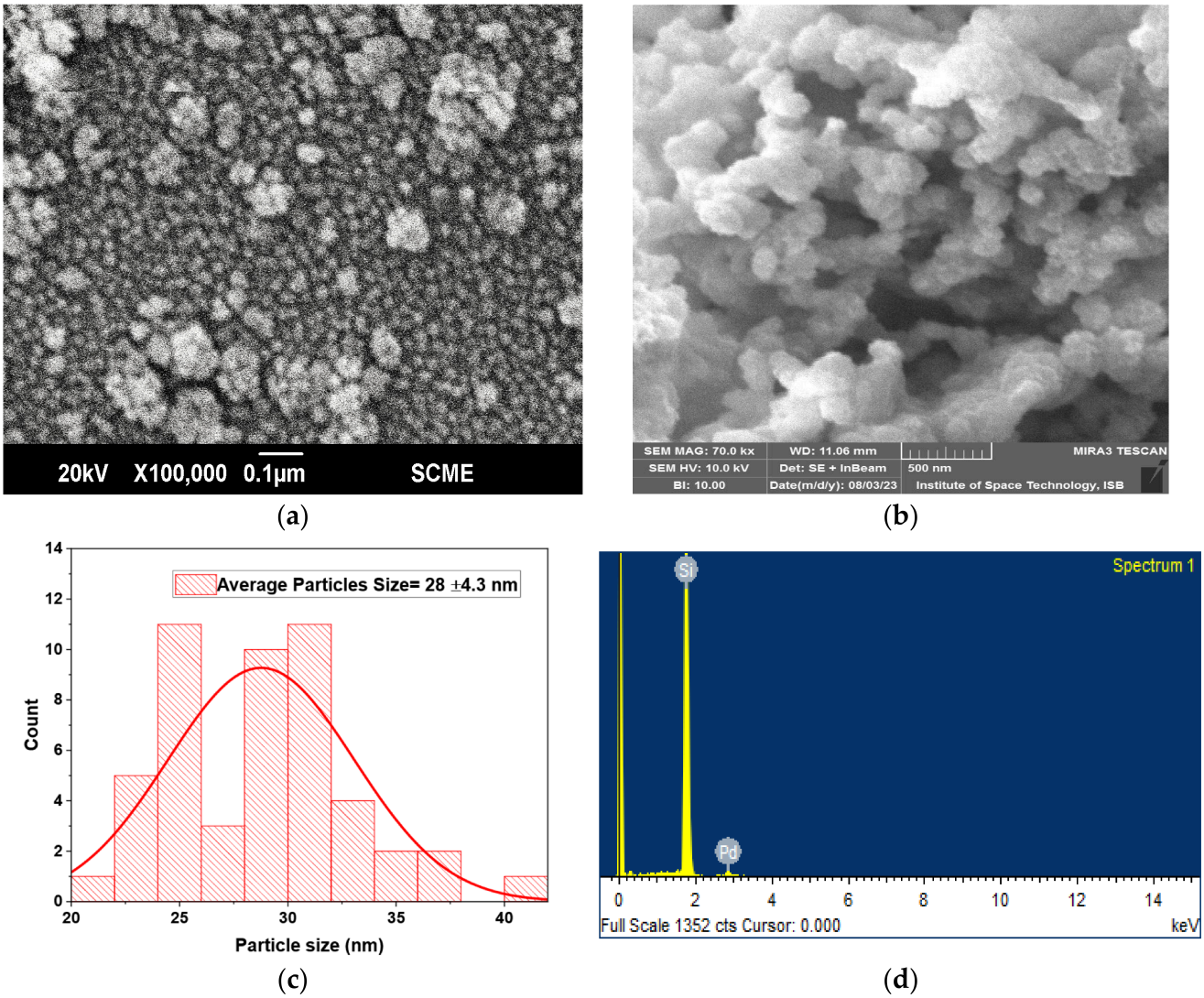


Figure 8. (**a**) SEM images of the S1 sample and (**b**) the S2 sample. (**c**) Particle size distribution histogram of the S1 sample. (**d**) EDX spectrum of the S1 sample.

The crystalline nature and phase composition of the synthesized Pd nanoparticles were investigated using X-ray diffraction (XRD). As shown in Figure 9, two distinct diffraction peaks are observed at 2θ values of 40.1° and 46.3°, which can be indexed to the (111) and (200) planes, respectively, of face-centered cubic (fcc) metallic Pd (JCPDS No. 87-0641). These characteristic reflections support the formation of crystalline metallic Pd^0 and are consistent with the metallic Pd detected by EDX analysis. A peak at approximately 2θ = 38.4° was also observed; however, this feature does not correspond to the characteristic reflections of fcc Pd and was therefore not assigned to the synthesized Pd nanoparticles. It may originate from the sample holder, substrate, or measurement background associated with the

XRD measurement. The remaining minor features in the diffraction pattern are relatively broad and poorly resolved and were therefore not assigned to specific crystalline phases.

The findings of these characterization techniques demonstrate that colloidal Pd NPs have been successfully synthesized using the PLI technique. The formation of Pd NPs in the present PLI system is governed by a series of plasma-induced physical and chemical reactions taking place in the plasma phase, at the plasma–liquid interface, and in the bulk solution [61]. The OES results presented in this study provide direct evidence of the reactive plasma environment responsible for the reduction of Pd ions and subsequent Pd NP formation.

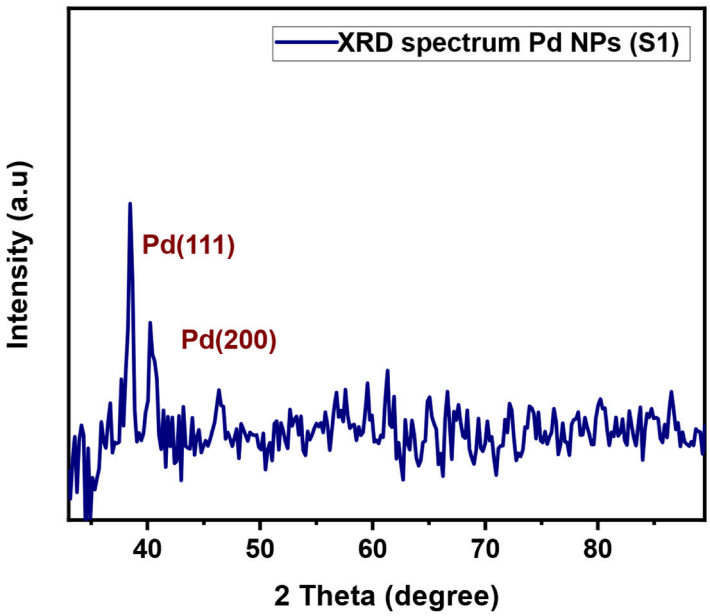


Figure 9. XRD pattern of the synthesized Pd NPs (S1 sample).

The emission spectra (Figure 1) confirm the presence of excited argon states along with OH radicals and molecular nitrogen emissions, demonstrating that excited plasma species are continuously generated during the discharge. Moreover, the increase in UV_a, UV_b, and UV_c intensities with an increasing discharge current indicates enhanced excitation processes within the plasma. When atmospheric-pressure argon plasma interacts with the aqueous precursor solution, energetic electrons are injected across the plasma–liquid interface, which leads to the formation of hydrated electrons.

$$H_2O + e^- \rightarrow e^-_{aq}$$

The solvated electrons have one of the highest reduction potentials among aqueous reducing species, making them highly effective reducing agents for noble metal ions [62]. As a result, Pd^{2+} ions originating from chloropalladic acid are directly reduced to metallic palladium atoms (Pd monomers).

$$Pd^{2+} + 2e^- \rightarrow Pd^0$$

This direct electron-driven reduction pathway is generally considered the dominant mechanism during the initial stages of plasma-assisted metal NP synthesis [58,62].

Besides electron injection, energetic plasma electrons and UV photons continuously dissociate water molecules, producing hydroxyl radicals that play a crucial role in the synthesis process [63,64].

$$e^- + H_2O \rightarrow H + OH$$

$$UV + H_2O^* \rightarrow OH + H$$

The experimentally observed increase in OH emission intensity demonstrates that water dissociation becomes increasingly efficient with the discharge current. The recombination of OH radicals produces hydrogen peroxide:

$$2OH^* \rightarrow H_2O_2$$

which represents a long-lived reactive species in plasma-treated liquids and is a very strong reducing agent [63,65]. It further participates in the reduction of palladium ions according to:

$$Pd^{2+} + H_2O_2 \rightarrow Pd^0 + O_2 + 2H^+$$

Therefore, both solvated electrons and plasma-generated secondary reducing species contribute to the conversion of Pd^{2+} into Pd metal monomers. These monomers subsequently aggregate, initiating the nucleation process and driving the growth of nanoparticles (NPs) [66]. D-fructose acts as a green stabilizing agent during the synthesis by forming a protective organic shell around Pd NPs. This coating reduces surface energy and suppresses particle aggregation, thereby controlling the size of NPs [67,68].

The plasma diagnostics reveal that an increasing discharge current simultaneously increases UV intensity, OH emission intensity, and T_g, while also decreasing T_e, which indicates a high flux of reducing species available for reduction. However, if plasma exposure continues under highly energetic conditions, the continuous generation of Pd atoms along with elevated T_g may accelerate post-nucleation growth through particle coalescence or Ostwald's ripening. Consequently, the particle size is governed not only by the nucleation rate but also by subsequent growth kinetics.

2.3. Catalytic Activity of Pd NPs

The catalytic activity of synthesized Pd NPs was studied for the reduction of 4-nitrophenol (4-NP), methyl orange (MO), and Congo red (CR). For the reduction of 4-NP, 30 µL of Pd NPs with a molarity of 0.4 mM (S1 sample) were added to a quartz cuvette containing 3 mL of 4-NP solution (1×10^{-4} M) and 1 mL of $NaBH_4$ (0.1 M). The Pd NPs with a smaller size distribution (S1) were used for catalysis, as higher catalytic activity is exhibited by small NPs due to an increased number of active sites on the surface. Similarly, for the catalytic reduction of MO and CR, 30 µL of Pd NPs were added to two quartz cuvettes containing 3 mL MO (0.05×10^{-3} M) and CR (1×10^{-4} M), along with 1 mL $NaBH_4$ (0.1 M), respectively.

To monitor the progress of reduction, UV–Vis spectroscopy was employed, and the absorption spectra of the solution were recorded at equal time intervals. The dye molecules have clear absorption peaks in the UV–Vis spectra and do not overlap with the Pd NP spectra, thereby enabling the investigation of catalytic activity. To evaluate the background reduction of the dyes by $NaBH_4$ in the absence of Pd NPs, control experiments were performed for all three dyes (4-nitrophenol, methyl orange, and Congo red) using the same experimental conditions as the catalytic experiments, but without adding Pd NPs. The UV–Vis spectra of the dye + $NaBH_4$ solutions were recorded over 50 min. No considerable change in the characteristic absorbance of any of the three dyes was observed even after 50 min, indicating a negligible reduction in the absence of the Pd catalyst (Figures 10a, 11a and 12a). $NaBH_4$ was used as the reductant in the catalytic performance experiments only; it was not added during Pd nanoparticle synthesis.

The reduction of these molecules by sodium borohydride ($NaBH_4$) in the presence of synthesized Pd NPs was successfully catalyzed. Consequently, the decolorization of the dye solutions was observed in all cases.

2.4. Catalytic Reduction of 4-NP

4-Nitrophenol is a phenolic compound used in the manufacturing of drugs, pesticides, and dyes. The accumulation of 4-NP in the environment occurs through different channels and waste streams, causing environmental damage [69]. The model reaction of the reduction of 4-NP can be used to study the catalytic efficiency of different types of NPs. The reduction of 4-NP to 4-AP in the presence of $NaBH_4$ is thermodynamically favorable. However, it does not take place in the absence of a catalyst, as a large kinetic barrier exists due to the potential difference between the donor and acceptor molecules [70]. The addition of Pd NPs as nanocatalysts enables the charge transfer between the molecules. The reduction of 4-NP to 4-AP occurs via the formation of 4-nitrophenolate ions, which converts the solution from colorless to a bright yellow color.

The absorption peak of 4-NP in the UV–Vis spectrum is at 317 nm. However, in the presence of $NaBH_4$, it is shifted to 400 nm due to the formation of 4-nitrophenolate ions. As a control experiment, the reduction of 4-NP in the presence of $NaBH_4$ without Pd NPs was monitored for 50 min (Figure 10a). Only a minor change in the absorption intensity at 400 nm was observed during this period, indicating a negligible background reduction of 4-NP by $NaBH_4$ alone. In contrast, Figure 10b shows the reduction of 4-NP with time in the presence of Pd NPs as the catalyst. It can be observed that the absorption peak of 4-NP at 400 nm begins to decay with an increase in time, and another peak corresponding to 4-aminophenol (4-AP) begins to rise at 300 nm. Hence, it was evident that Pd NPs efficiently catalyzed the conversion of 4-NP to 4-AP.

The reduction reaction was completed in 12 min, as the color of the solution completely changed from bright yellow to colorless. As the concentration of $NaBH_4$ (0.1 M) used was much higher than that of 4-NP, it can be considered that the concentration of $NaBH_4$ remained constant throughout the reaction. Therefore, the reaction followed pseudo-first-order kinetics, which can be expressed mathematically as:

$$\ln\left(\frac{C_t}{C_o}\right) = kt$$

where C_t is the concentration of 4-NP at time t, C_o is the concentration of 4-AP at time 0, k is the apparent rate constant, and t represents time [71]. The plot of $\ln(C_t/C_o)$ versus time t is shown in Figure 10d and is a straight line. The apparent rate constant can be calculated from the slope of the graph and is determined to be 0.2508 min^{-1}.

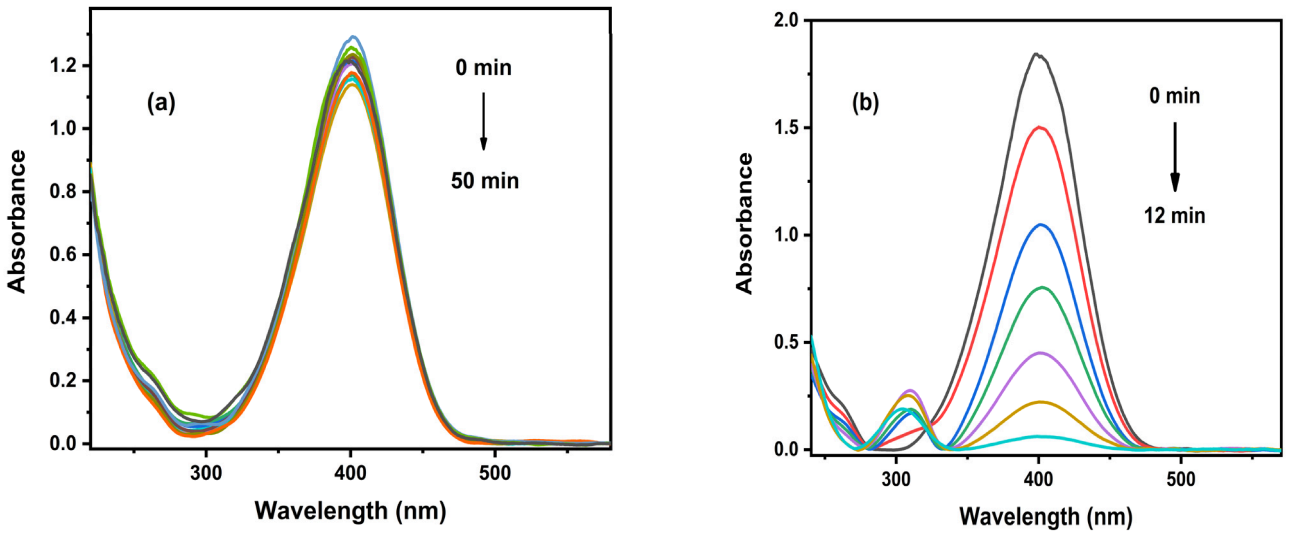


Figure 10. *Cont.*

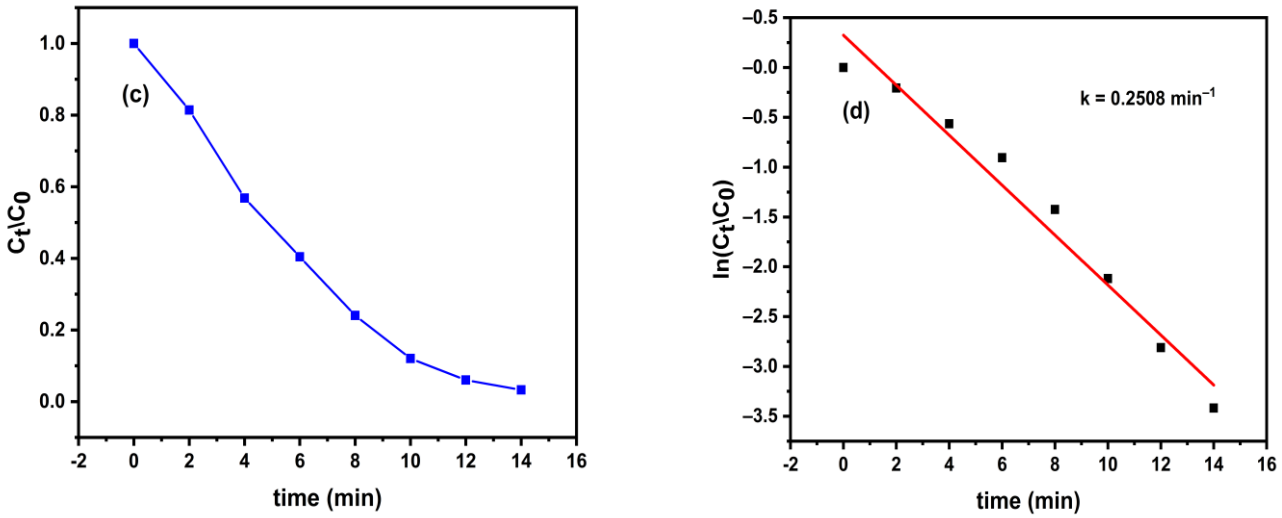


Figure 10. (**a**) Control experiment of 4-NP reduction in the absence of Pd NPs. (**b**) Catalytic reduction of 4-NP using synthesized Pd NPs. (**c**) C_t/C_o vs. time t plot. (**d**) $\ln(C_t/C_o)$ vs. time t plot of the reaction.

2.5. Catalytic Reduction of MO

Methyl orange is a water-soluble azo dye that is used in the textile, paint, and paper industries. The degradation of MO into reduced products has been studied using the synthesized Pd NPs (shown in Figure 11a,b). MO shows an absorption peak at 465 nm in the UV–Vis spectrum. It was observed that with an increase in time, there was a successive decrease in the 465 nm peak, and the decolorization of the solution occurred. On the other hand, there was an increase in the product peaks at 203 nm and 250 nm with increasing time, and the degradation of MO into reduced products occurred within 5 min.

Figure 11c shows the relationship of C_t/C_o as a function of time, while Figure 11d displays the correlation of the $\ln(C_t/C_o)$ versus time plot of the reaction, which was found to be linear. The apparent rate constant value of the reaction was calculated to be 0.6346 min^{-1}.

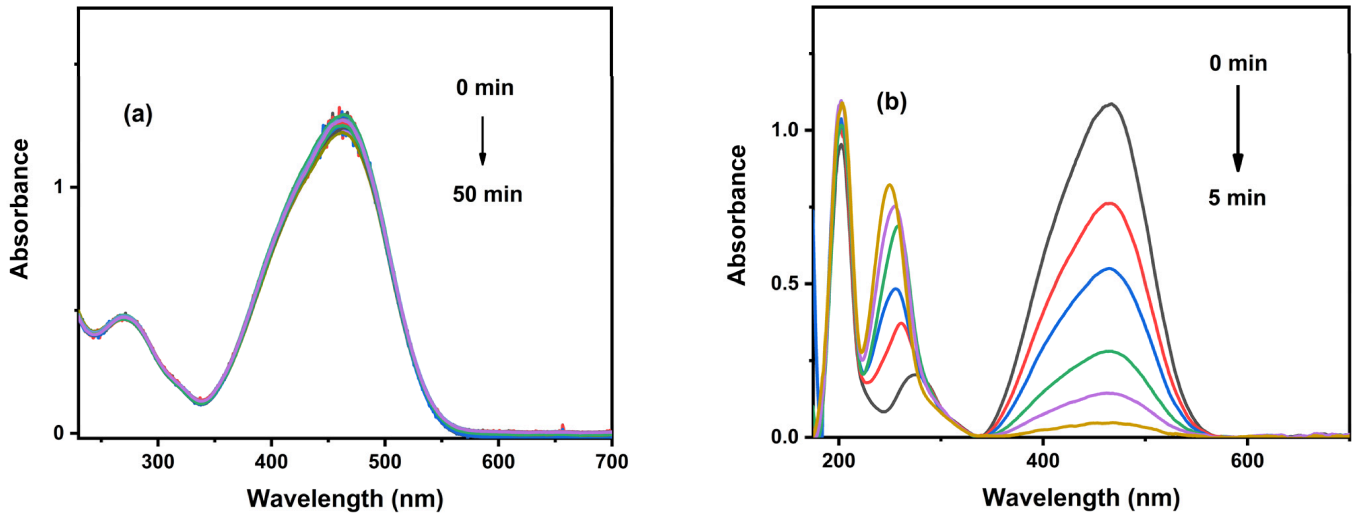


Figure 11. *Cont.*

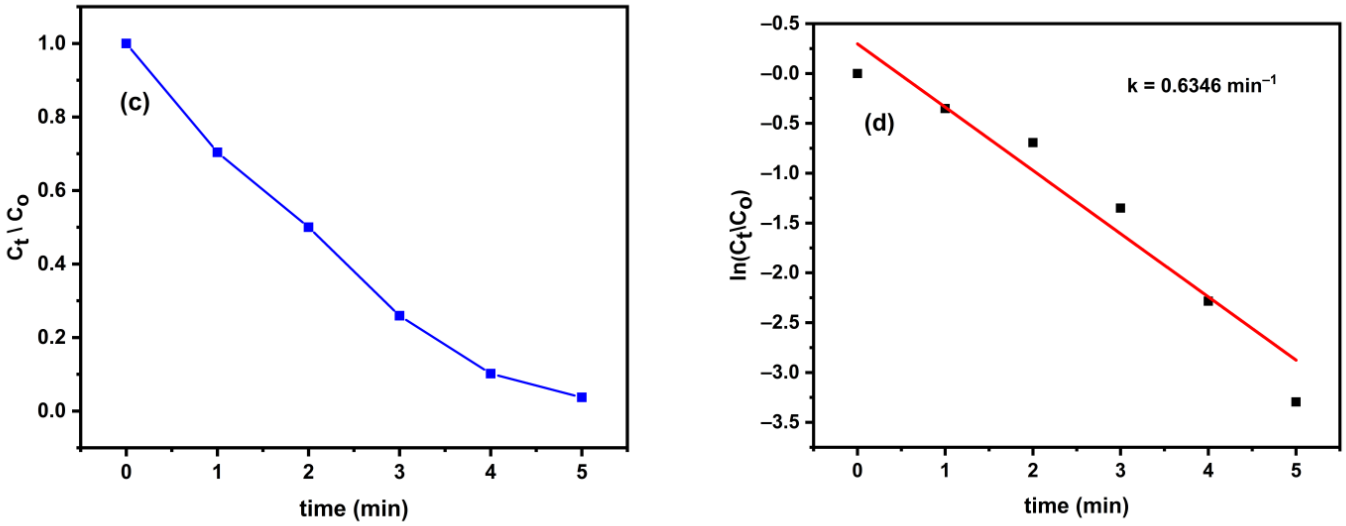


Figure 11. (**a**) Control experiment of MO reduction in the absence of Pd NPs. (**b**) Catalytic reduction of MO using synthesized Pd NPs. (**c**) C_t/C_o vs. time t plot. (**d**) $\ln(C_t/C_o)$ vs. time t plot of the reaction.

2.6. Catalytic Reduction of CR

The catalytic efficiency of Pd NPs was also investigated for the degradation of CR. It is another azo dye that has carcinogenic and mutagenic properties [72]. It has naphthalene and benzene rings and shows two absorption peaks at 494 nm and 340 nm in aqueous media, corresponding to (N=N) bonds [73]. Figure 12a,b depict the degradation of CR with the addition of Pd NPs. The absorption peaks of CR gradually decreased, while two new peaks at 247 nm and 290 nm emerged with an increase in time. The color of the solution also changed from dark red to colorless. It can be deduced that Pd NP catalysts accelerated the degradation of CR, which resulted in the breakage of double azo bonds, leading to the formation of aromatic amines as reduced products.

The characteristic CR absorption bands were no longer observed after 10 min. Figure 12c depicts the relationship between C_t/C_o and time, whereas Figure 12d is the natural log of C_t/C_o and shows a linear correlation of $\ln(C_t/C_o)$ versus time t. The rate constant k of the reaction was determined to be 0.3416 min^{-1}.

The reduction of these molecules conducted at room temperature showed high values of rate constants, depicting remarkable catalytic efficiency, as 12×10^{-9} mol of synthesized Pd NPs were added to the solutions as catalysts. The catalytic degradation in the presence of d-fructose-stabilized Pd NPs proceeds through a heterogeneous surface-mediated reduction mechanism, as shown in Figure 13. Although $NaBH_4$ is a strong reducing agent, its direct reaction with azo dyes such as MO and CR is kinetically hindered due to the presence of a large potential difference between the donor (BH_4^-) and acceptor (dye) molecules [70]. Pd NPs overcome this limitation by providing a large number of active surface sites where both reducing agents and dye molecules can simultaneously adsorb [74,75]. Additionally, the d-fructose coating on Pd NPs also plays an important role in sustaining the catalytic efficiency of Pd NPs. D-fructose forms a very thin, uniform layer on the Pd surface, preserving the dispersion of NPs while still allowing reactant molecules to access the catalytic sites [68].

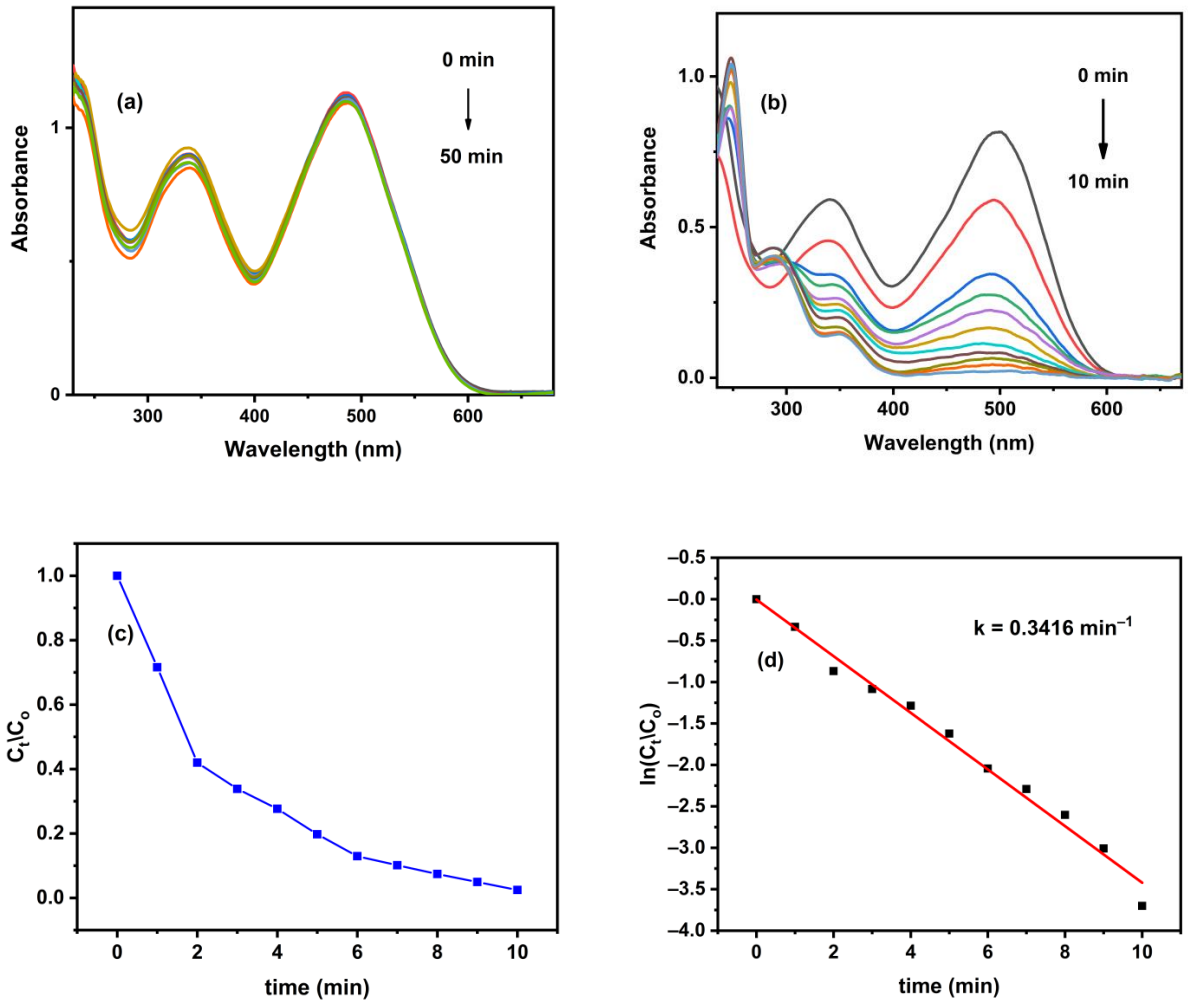


Figure 12. (**a**) Control experiment of CR reduction in the absence of Pd NPs. (**b**) Catalytic reduction of CR using synthesized Pd NPs. (**c**) C_t/C_o vs. time t plot. (**d**)$\ln(C_t/C_o)$ vs. time t plot of the reaction.

Upon adsorption, BH_4^- ions decompose on the Pd NP surface to generate active hydrogen species, which are subsequently transferred to the azo (N=N) bonds of the dye molecules. The Pd NPs act as an electron relay, which lowers the activation energy for the reduction reaction. This process results in the cleavage of azo bonds and the formation of corresponding byproducts. For MO, reductive cleavage has been reported to yield products such as sulfanilic acid and N, N-dimethylaniline, while the reductive cleavage of CR can produce benzidine-related aromatic amines and naphthylamine derivatives. A similar catalytic pathway is observed for the model reaction of 4-NP, where a nitro group is reduced to an amino group to form 4-AP [76].

After the reduction reaction, the degraded products desorb from the Pd NP surface, leaving active sites available for subsequent catalytic cycles. Overall, the catalytic degradation mechanism, adsorption of reactants, surface-mediated electron and hydrogen transfer, reductive cleavage of azo bonds, and catalyst regeneration make Pd NPs highly effective catalysts for the reduction and decolorization of hazardous azo dyes in aqueous environments.

Table 1 summarizes reported apparent rate constants for the catalytic reduction of 4-NP, MO, and CR using Pd-based catalysts and places the present results in the context of the previously reported studies. These rate constants depend on substrate and $NaBH_4$ concentrations, catalyst loading, temperature, and other experimental conditions. The comparison is contextual rather than a direct ranking of intrinsic catalytic activity.

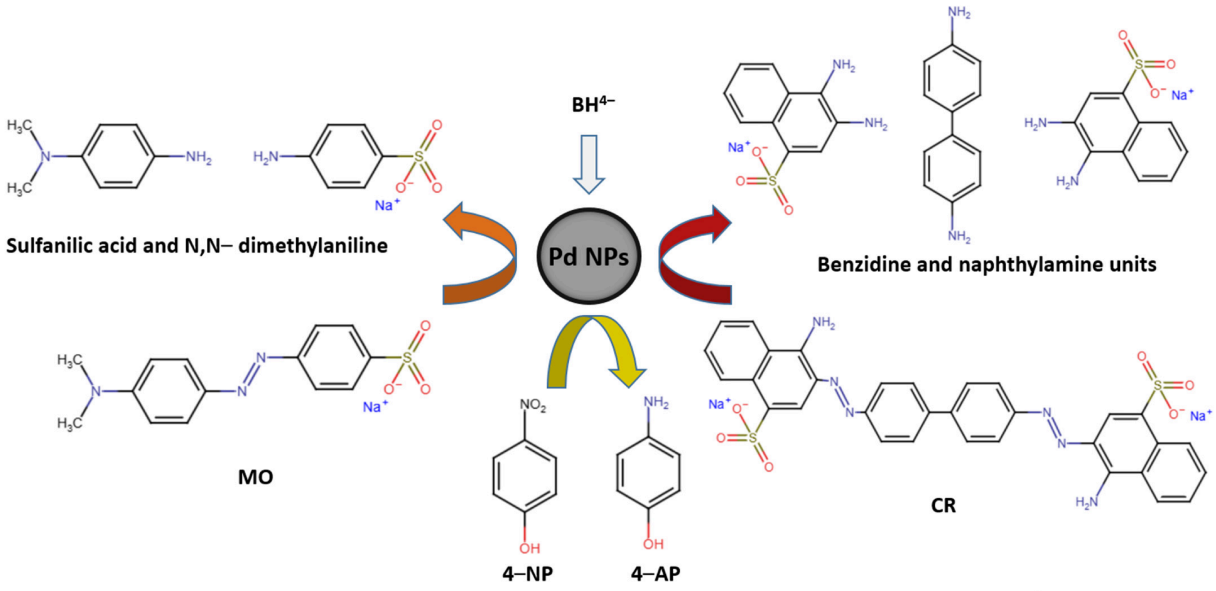


Figure 13. Schematic diagram of the catalytic reduction of 4-NP, MO, and CR.

Table 1. Comparison of rate constants for catalytic reduction using synthesized Pd NPs with the previously reported literature.

Dye	Catalyst	Rate Constant k (min^{-1})	Reference
4-NP	Spindle-like Pd NPs	0.1395	[77]
	Pd NPs	0.1806	[78]
	Pd NPs	1.65×10^{-2}	[20]
	Pd NPs	0.2508	Present work
MO	PVDF/β-CD-P	0.1700	[79]
	Pd NPs	0.1576	[80]
	nZVI/Pd NPs	0.0721	[81]
	Pd NPs	0.6346	Present work
CR	Pd NPs	0.1614	[78]
	Pd NPs	0.8952×10^{-3}	[82]
	CT-supported Pd	3.8×10^{-3}	[83]
	Pd NPs	0.3416	Present work

3. Experimental Setup

The schematic diagram of the PLI system used for the synthesis of Pd NPs is shown in Figure 14. A detailed description of the plasma discharge system can be found in our previous research paper [84]. To give a brief account, microplasma was generated above the electrolyte solution containing the precursors, i.e., H_2PdCl_4 and d-fructose, (Sigma-Aldrich, St. Louis, MO, USA) in a glass beaker. For that purpose, a stainless steel capillary tube with a 10 cm length and a 0.75 µm inner diameter was used as the cathode. The capillary tube was placed 2 mm above the precursor solution, and argon gas was made to pass through it as a working gas. The flow rate of Ar gas was maintained at 100 SCCM using a gas flow meter. A platinum electrode was submerged in the electrolyte solution, which acted as the anode. The plasma discharge was generated at atmospheric pressure by providing the discharge current through a negatively biased DC power supply. Optical emission spectroscopy (OES) was employed to characterize plasma-generated reactive species. Emission spectra were acquired using a high-resolution spectrometer. Time-averaged plasma emission spectra were recorded using a five-leg optical fiber (400 µm width each) coupled to the spectrometer. The discharge current of 5 mA was applied between the electrodes using a 100 kΩ ballast

resistor while a DC voltage of 8 kV was maintained. The setup was optimized at 8 kV and 5 mA for the treatment. After several minutes of plasma treatment, 20 mL of solution containing the synthesized Pd NPs was collected.

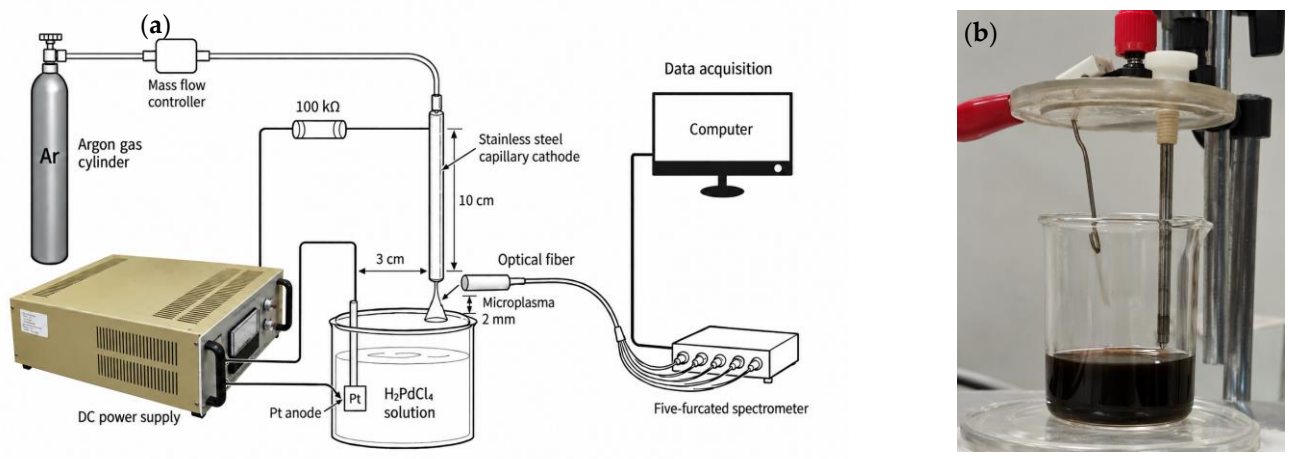


Figure 14. (**a**) Schematics of the argon microplasma–liquid setup for Pd NP synthesis. (**b**) Real-time photo, taken with a Vivo V40e camera.

4. Conclusions

Atmospheric-pressure plasma–liquid interactions provide a scalable route to colloidal NPs, but controlling nucleation and growth under ambient microplasma remains challenging. Here, we report single-step microplasma synthesis of d-fructose-coated Pd NPs using a capillary cathode and a solution anode configuration under DC operation. The thermo-physical parameters of the plasma, electron temperature T_e, and gas temperature T_g, which control reduction kinetics and growth conditions, have been studied using OES. UV–Vis tracking indicates the rapid conversion of Pd^{2+} ions into Pd^0, with the growth of most NPs completed within 30 min of plasma treatment. SEM and EDX analysis confirm the formation of metallic Pd nanostructures with predominantly spherical particles. An optimized discharge current of 5 mA provided a favorable reactive environment, enabling the efficient electron-driven reduction of Pd ions while limiting excessive thermal effects. It was noted that the stability and uniformity of Pd NPs may be enhanced by increasing the d-fructose concentration. The catalytic studies of the synthesized Pd NPs showed excellent efficiency in the catalytic reduction of dyes. The rate constants for the reduction of 4-NP, MO, and CR were determined to be 0.2508 min^{-1}, 0.6346 min^{-1}, and 0.3416 min^{-1}, respectively. These findings demonstrated PLIs as a controllable route for aqueous Pd NP synthesis without a separately added chemical reductant and provided insights into the plasma-driven mechanisms governing NP formation. The overall environmental performance of this route remains to be established through the assessment of precursor hazards, energy and material consumption, product recovery, and waste management.

Author Contributions: Conceptualization, S.I. and N.U.R.; methodology, S.I., W.A., A.N.Q., N.W., N.U.R. and T.R.; validation, W.A., N.W., N.U.R., Y.Y. and T.R.; formal analysis, S.I., A.N.Q., N.W., Y.Y. and T.R.; investigation, S.I. and A.N.Q.; data curation, S.I. and A.N.Q.; resources, W.A. and N.U.R.; writing—original draft preparation, S.I. and A.N.Q.; writing—review and editing, W.A., N.W., N.U.R., Y.Y. and T.R.; visualization, S.I. and A.N.Q.; supervision, W.A., N.U.R. and T.R.; project administration, N.U.R.; funding acquisition, N.U.R. and T.R. All authors have read and agreed to the published version of the manuscript.

Funding: This research received the financial support (QU-APC-2026) of the Deanship of Graduate Studies and Scientific Research at Qassim University (https://www.qu.edu.sa).

Data Availability Statement: The data that support the findings of this study are available from the corresponding author upon reasonable request.

Acknowledgments: The Researchers would like to thank the Deanship of Graduate Studies and Scientific Research at Qassim University (https://www.qu.edu.sa) for financial support (QU-APC-2026).

Conflicts of Interest: The authors declare no conflict of interest.

References

1. Trügler, A. *Optical Properties of Metallic Nanoparticles*; Springer: Berlin/Heidelberg, Germany, 2011.
2. Lue, J.-T. A review of characterization and physical property studies of metallic nanoparticles. *J. Phys. Chem. Solids* **2001**, *62*, 1599–1612. [CrossRef]
3. Zehani, K.; Bez, R.; Boutahar, A.; Hlil, E.K.; Lassri, H.; Moscovici, J.; Mliki, N.; Bessais, L. Structural, magnetic, and electronic properties of high moment FeCo nanoparticles. *J. Alloys Compd.* **2014**, *591*, 58–64. [CrossRef]
4. Lin, X.-M.; Samia, A.C. Synthesis, assembly and physical properties of magnetic nanoparticles. *J. Magn. Magn. Mater.* **2006**, *305*, 100–109. [CrossRef]
5. Doria, G.; Conde, J.; Veigas, B.; Giestas, L.; Almeida, C.; Assunção, M.; Rosa, J.; Baptista, P.V. Noble metal nanoparticles for biosensing applications. *Sensors* **2012**, *12*, 1657–1687. [CrossRef] [PubMed]
6. Norouzi, H.; Khoshgard, K.; Akbarzadeh, F. In vitro outlook of gold nanoparticles in photo-thermal therapy: A literature review. *Lasers Med. Sci.* **2018**, *33*, 917–926. [CrossRef] [PubMed]
7. Chandrakala, V.; Aruna, V.; Angajala, G. Review on metal nanoparticles as nanocarriers: Current challenges and perspectives in drug delivery systems. *Emergent Mater.* **2022**, *5*, 1593–1615. [CrossRef] [PubMed]
8. Chen, S.; Yuan, R.; Chai, Y.; Hu, F. Electrochemical sensing of hydrogen peroxide using metal nanoparticles: A review. *Microchim. Acta* **2013**, *180*, 15–32. [CrossRef]
9. Favier, I.; Madec, D.; Teuma, E.; Gómez, M. Palladium nanoparticles applied in organic synthesis as catalytic precursors. *Curr. Org. Chem.* **2011**, *15*, 3127–3174. [CrossRef]
10. Chen, A.; Ostrom, C. Palladium-based nanomaterials: Synthesis and electrochemical applications. *Chem. Rev.* **2015**, *115*, 11999–12044. [CrossRef] [PubMed]
11. Celebi, M.; Yurderi, M.; Bulut, A.; Kaya, M.; Zahmakiran, M. Palladium nanoparticles supported on amine-functionalized SiO_2 for the catalytic hexavalent chromium reduction. *Appl. Catal. B Environ.* **2016**, *180*, 53–64. [CrossRef]
12. Tsuji, J. *Palladium Reagents and Catalysts: Innovations in Organic Synthesis*; John Wiley & Sons: New York, NY, USA, 1995.
13. Toebes, M.L.; van Dillen, A.J.; de Jong, K.P. Synthesis of supported palladium catalysts. *J. Mol. Catal. A Chem.* **2001**, *173*, 75–98. [CrossRef]
14. Chaplin, B.P.; Reinhard, M.; Schneider, W.F.; Schüth, C.; Shapley, J.R.; Strathmann, T.J.; Werth, C.J. Critical review of Pd-based catalytic treatment of priority contaminants in water. *Environ. Sci. Technol.* **2012**, *46*, 3655–3670. [CrossRef] [PubMed]
15. Varma, R.S. Greener approach to nanomaterials and their sustainable applications. *Curr. Opin. Chem. Eng.* **2012**, *1*, 123–128. [CrossRef]
16. Khodadadi, B.; Bordbar, M.; Nasrollahzadeh, M. *Achillea millefolium* L. extract mediated green synthesis of waste peach kernel shell supported silver nanoparticles: Application of the nanoparticles for catalytic reduction of a variety of dyes in water. *J. Colloid Interface Sci.* **2017**, *493*, 85–93. [CrossRef] [PubMed]
17. Centi, G.; Ciambelli, P.; Perathoner, S.; Russo, P. Environmental catalysis: Trends and outlook. *Catal. Today* **2002**, *75*, 3–15. [CrossRef]
18. de Lima, R.O.A.; Bazo, A.P.; Salvadori, D.M.F.; Rech, C.M.; de Oliveira, D.P.; Umbuzeiro, G.A. Mutagenic and carcinogenic potential of a textile azo dye processing plant effluent that impacts a drinking water source. *Mutat. Res. Genet. Toxicol. Environ. Mutagen.* **2007**, *626*, 53–60. [CrossRef] [PubMed]
19. Wang, Z.; Lü, S.; Yang, F.; Kabir, S.M.F.; Mahmud, S.; Liu, H. Hyaluronate macromolecules reduced-stabilized colloidal palladium nanocatalyst for azo contaminated wastewater treatment. *Colloids Surf. A Physicochem. Eng. Asp.* **2021**, *628*, 127345. [CrossRef]
20. Islam, M.T.; Saenz-Arana, R.; Wang, H.; Bernal, R.; Noveron, J.C. Green synthesis of gold, silver, platinum, and palladium nanoparticles reduced and stabilized by sodium rhodizonate and their catalytic reduction of 4-nitrophenol and methyl orange. *New J. Chem.* **2018**, *42*, 6472–6478. [CrossRef]
21. Lebaschi, S.; Hekmati, M.; Veisi, H. Green synthesis of palladium nanoparticles mediated by black tea leaves (*Camellia sinensis*) extract: Catalytic activity in the reduction of 4-nitrophenol and Suzuki-Miyaura coupling reaction under ligand-free conditions. *J. Colloid Interface Sci.* **2017**, *485*, 223–231. [CrossRef] [PubMed]
22. Karousis, N.; Tsotsou, G.-E.; Evangelista, F.; Rudolf, P.; Ragoussis, N.; Tagmatarchis, N. Carbon nanotubes decorated with palladium nanoparticles: Synthesis, characterization, and catalytic activity. *J. Phys. Chem. C* **2008**, *112*, 13463–13469. [CrossRef]

23. Ganji, S.; Bukya, P.; Liu, Z.; Rao, K.S.R.; Burri, D.R. A carboxylic acid functionalized SBA-15 supported Pd nanocatalyst: An efficient catalyst for hydrogenation of nitrobenzene to aniline in water. *New J. Chem.* **2019**, *43*, 11871–11875. [CrossRef]
24. Liu, J.; He, F.; Gunn, T.M.; Zhao, D.; Roberts, C.B. Precise seed-mediated growth and size-controlled synthesis of palladium nanoparticles using a green chemistry approach. *Langmuir* **2009**, *25*, 7116–7128. [CrossRef] [PubMed]
25. Sun, Y.; Zhang, L.; Zhou, H.; Zhu, Y.; Sutter, E.; Ji, Y.; Rafailovich, M.H.; Sokolov, J.C. Seedless and templateless synthesis of rectangular palladium nanoparticles. *Chem. Mater.* **2007**, *19*, 2065–2070. [CrossRef]
26. Roy, P.S.; Bagchi, J.; Bhattacharya, S.K. Synthesis of polymer-protected palladium nanoparticles of contrasting electrocatalytic activity: A comparative study with respect to reflux time and reducing agents. *Colloids Surf. A Physicochem. Eng. Asp.* **2010**, *359*, 45–52. [CrossRef]
27. Qiu, X.-F.; Xu, J.-Z.; Zhu, J.-M.; Zhu, J.-J.; Xu, S.; Chen, H.-Y. Controllable synthesis of palladium nanoparticles via a simple sonoelectrochemical method. *J. Mater. Res.* **2003**, *18*, 1399–1404. [CrossRef]
28. Borisov, R.V.; Belousov, O.V.; Likhatski, M.N.; Zhizhaev, A.M.; Kirik, S.D. Hydrothermal synthesis of Ir and Ir—Pd nanoparticles on carbon nanotubes. *Russ. Chem. Bull.* **2022**, *71*, 1164–1172. [CrossRef]
29. Kozłowski, M.; Czerwosz, E.; Dłużewski, P.; Kowalska, E.; Radomska, J.; Wronka, H. Nanostructural C-Pd coatings obtained in 2-steps PVD/CVD technological process. *J. Achiev. Mater. Manuf. Eng.* **2009**, *37*, 304–308.
30. Boutinguiza, M.; Meixus, M.; del Val, J.; Riveiro, A.; Comesaña, R.; Lusquiños, F.; Pou, J. Synthesis and characterization of Pd nanoparticles by laser ablation in water using nanosecond laser. *Phys. Procedia* **2016**, *83*, 36–45. [CrossRef]
31. Hazarika, M.; Borah, D.; Bora, P.; Silva, A.R.; Das, P. Biogenic synthesis of palladium nanoparticles and their applications as catalyst and antimicrobial agent. *PLoS ONE* **2017**, *12*, e0184936. [CrossRef] [PubMed]
32. Mariotti, D.; Sankaran, R.M. Perspectives on atmospheric-pressure plasmas for nanofabrication. *J. Phys. D Appl. Phys.* **2011**, *44*, 174023. [CrossRef]
33. Darwish, M.; Mafla-Gonzalez, C.; Kolenovic, B.; Deremer, A.; Centeno, D.; Liu, T.; Kim, D.-Y.; Cattabiani, T.; Drwiega, T.J.; Kumar, I.; et al. Rapid synthesis of metal nanoparticles using low-temperature, low-pressure argon plasma chemistry and self-assembly. *Green Chem.* **2022**, *24*, 8142–8154. [CrossRef] [PubMed]
34. Vons, V.A.; Creyghton, Y.; Schmidt-Ott, A. Nanoparticle production using atmospheric pressure cold plasma. *J. Nanopart. Res.* **2006**, *8*, 721–728. [CrossRef]
35. Wang, Z.; Zhu, Y. A simple plasma reduction for synthesis of Au and Pd nanoparticles at room temperature. *Chin. J. Chem. Eng.* **2015**, *23*, 1060–1063. [CrossRef]
36. Liu, Y.; Bai, X. Argon glow discharge plasma-reduced palladium nanoparticles supported on activated carbon for Suzuki and Heck coupling reactions. *Appl. Organomet. Chem.* **2017**, *31*, e3561. [CrossRef]
37. Zhao, Q.; Bu, D.; Li, Z.; Zhang, X.; Di, L. Cold plasma preparation of Pd/graphene catalyst for reduction of p-nitrophenol. *Nanomaterials* **2021**, *11*, 1341. [CrossRef] [PubMed]
38. Di, L.; Zhang, X.; Lee, B.; Lu, P.; Ahn, W.-S.; Park, D.-W. Feasibility of atmospheric-pressure CO cold plasma for reduction of supported metal ions. *Plasma Chem. Plasma Process.* **2017**, *37*, 1535–1549. [CrossRef]
39. Pang, Y.; Li, H.; Hua, Y.; Zhang, X.; Di, L. Rapid Synthesis of Noble Metal Colloids by Plasma–Liquid Interactions. *Materials* **2024**, *17*, 987. [CrossRef] [PubMed]
40. Sauvageau, J.-F.; Turgeon, S.; Chevallier, P.; Fortin, M.-A. Colloidal suspensions of platinum group metal nanoparticles (Pt, Pd, Rh) synthesized by dielectric barrier discharge plasma (DBD). *Part. Part. Syst. Charact.* **2018**, *35*, 1700365. [CrossRef]
41. Dzimitrowicz, A.; Greda, K.; Lesniewicz, T.; Jamroz, P.; Nyk, M.; Pohl, P. Size-controlled synthesis of gold nanoparticles by a novel atmospheric pressure glow discharge system with a metallic pin electrode and a flowing liquid electrode. *RSC Adv.* **2016**, *6*, 80773–80783. [CrossRef]
42. Dzimitrowicz, A.; Jamroz, P.; Pogoda, D.; Nyk, M.; Pohl, P. Direct current atmospheric pressure glow discharge generated between a pin-type solid cathode and a flowing liquid anode as a new tool for silver nanoparticles production. *Plasma Process. Polym.* **2017**, *14*, 1600251. [CrossRef]
43. Peng, X. An essay on synthetic chemistry of colloidal nanocrystals. *Nano Res.* **2009**, *2*, 425–447. [CrossRef]
44. Janev, R.K.; Presnyakov, L.P.; Shevelko, V.P. *Physics of Highly Charged Ions*; Springer: Berlin/Heidelberg, Germany, 2012; Volume 13. [CrossRef]
45. Herzberg, G.; Mrozowski, S. Molecular spectra and molecular structure. I. Spectra of diatomic molecules. *Am. J. Phys.* **1951**, *19*, 390–391. [CrossRef]
46. Khatoon, N.; Yasin, H.M.; Younus, M.; Ahmed, W.; Rehman, N.U.; Zakaullah, M.; Iqbal, M.Z. Synthesis and spectroscopic characterization of gold nanoparticles via plasma-liquid interaction technique. *AIP Adv.* **2018**, *8*, 015130. [CrossRef]
47. Bruggeman, P.; Leys, C. Non-thermal plasmas in and in contact with liquids. *J. Phys. D Appl. Phys.* **2009**, *42*, 053001. [CrossRef]
48. Wang, J.; Wang, M.; Fang, J.; Xu, S.; Guo, Y.; Ding, K.; Shi, J. Plasma-activated water: Effects of gas–liquid interface interaction and discharge intensity on activation properties. *Phys. Plasmas* **2025**, *32*, 033505. [CrossRef]

49. Sun, B.; Kunitomo, S.; Igarashi, C. Characteristics of ultraviolet light and radicals formed by pulsed discharge in water. *J. Phys. D Appl. Phys.* **2006**, *39*, 3814–3819. [CrossRef]
50. Rehman, N.U.; Khan, F.U.; Naveed, M.A.; Zakaullah, M. Determination of excitation temperature and vibrational temperature of the N2 (C 3Πu, ν′) state in Ne–N2 RF discharges. *Plasma Sources Sci. Technol.* **2008**, *17*, 025005. [CrossRef]
51. Babayan, S.E.; Jeong, J.Y.; Tu, V.J.; Park, J.; Selwyn, G.S.; Hicks, R.F. Deposition of silicon dioxide films with an atmospheric-pressure plasma jet. *Plasma Sources Sci. Technol.* **1998**, *7*, 286–288. [CrossRef]
52. Laux, C.O.; Spence, T.G.; Kruger, C.H.; Zare, R.N. Optical diagnostics of atmospheric pressure air plasmas. *Plasma Sources Sci. Technol.* **2003**, *12*, 125–138. [CrossRef]
53. Sarani, A.; Nikiforov, A.Y.; Leys, C. Atmospheric pressure plasma jet in Ar and Ar/H_2O mixtures: Optical emission spectroscopy and temperature measurements. *Phys. Plasmas* **2010**, *17*, 063504. [CrossRef]
54. Qadri, A.N.; Wali, N.; Farooq, M.; Rehman, N.U. Spectroscopic investigation of nanosecond pulsed discharges in underwater plasma for flowing water treatment applications. *J. Phys. D Appl. Phys.* **2025**, *58*, 265207. [CrossRef]
55. Wang, Q.; Koleva, I.; Donnelly, V.M.; Economou, D.J. Spatially resolved diagnostics of an atmospheric pressure direct current helium microplasma. *J. Phys. D Appl. Phys.* **2005**, *38*, 1690–1697. [CrossRef]
56. Farooq, M.; Ismail, S.; Rehman, N.U. Nanosecond pulsed plasma discharge for remediation of simulated wastewater containing thiazine and azo dyes as model pollutants. *J. Vac. Sci. Technol. A* **2023**, *41*, 013001. [CrossRef]
57. Silsby, J.A.; Dickenson, A.; Walsh, J.L.; Hasan, M.I. Resolving the spatial scales of mass and heat transfer in direct plasma sources for activating liquids. *Front. Phys.* **2022**, *10*, 1045196. [CrossRef]
58. Bruggeman, P.J.; Kushner, M.J.; Locke, B.R.; Gardeniers, J.G.E.; Graham, W.G.; Graves, D.B.; Hofman-Caris, R.C.H.M.; Maric, D.; Reid, J.P.; Ceriani, E.; et al. Plasma–liquid interactions: A review and roadmap. *Plasma Sources Sci. Technol.* **2016**, *25*, 053002. [CrossRef]
59. Bahrami, K.; Targhan, H. A new strategy to design a graphene oxide supported palladium complex as a new heterogeneous nanocatalyst and application in carbon–carbon and carbon-heteroatom cross-coupling reactions. *Appl. Organomet. Chem.* **2019**, *33*, e4842. [CrossRef]
60. Patel, J.; Němcová, L.; Maguire, P.; Graham, W.G.; Mariotti, D. Synthesis of surfactant-free electrostatically stabilized gold nanoparticles by plasma-induced liquid chemistry. *Nanotechnology* **2013**, *24*, 245604. [CrossRef] [PubMed]
61. Xie, P.; Qi, Y.; Wang, R.; Wu, J.; Li, X. Aqueous gold nanoparticles generated by AC and pulse-power-driven plasma jet. *Nanomaterials* **2019**, *9*, 1488. [CrossRef] [PubMed]
62. Blake, M. Atmospheric Pressure Plasmas at the Liquid Interface. Master's Thesis, University of York, York, UK, 2014.
63. Khatoon, N.; Ahmed, W.; Rehman, N.U. Spectroscopic analysis of gold nanoparticle synthesis using plasma liquid interaction technique. *Mater. Res. Express* **2019**, *6*, 095056. [CrossRef]
64. Yasin, H.M.; Ahmed, W.; Ali, A.; Bhatti, A.S.; Rehman, N.U. Micro-plasma assisted synthesis of multifunctional D-fructose coated silver nanoparticles. *Mater. Res. Express* **2019**, *6*, 1050a2. [CrossRef]
65. Van Gaens, W.; Iseni, S.; Schmidt-Bleker, A.; Weltmann, K.-D.; Reuter, S.; Bogaerts, A. Numerical analysis of the effect of nitrogen and oxygen admixtures on the chemistry of an argon plasma jet operating at atmospheric pressure. *New J. Phys.* **2015**, *17*, 033003. [CrossRef]
66. Wang, R.; Zuo, S.; Wu, D.; Zhang, J.; Zhu, W.; Becker, K.H.; Fang, J. Microplasma-assisted synthesis of colloidal gold nanoparticles and their use in the detection of cardiac troponin I (cTn-I). *Plasma Process. Polym.* **2015**, *12*, 380–391. [CrossRef]
67. Jung, S.C.; Park, Y.-K.; Jung, H.-Y.; Kim, S.C. Effect of stabilizing agents on the synthesis of palladium nanoparticles. *J. Nanosci. Nanotechnol.* **2017**, *17*, 2833–2836. [CrossRef] [PubMed]
68. Yasin, H.M.; Ahmed, W.; Rehman, N.U.; Majd, A.; Alkhedher, M.; Tag El Din, E.M. Plasma-Assisted Synthesis of Surfactant-Free and D-Fructose-Coated Gold Nanoparticles for Multiple Applications. *Materials* **2022**, *15*, 7579. [CrossRef] [PubMed]
69. Baselt, R. Encyclopedia of toxicology. *J. Anal. Toxicol.* **2014**, *38*, 464. [CrossRef]
70. Gangula, A.; Podila, R.; Ramakrishna, M.; Karanam, L.; Janardhana, C.; Rao, A.M. Catalytic reduction of 4-nitrophenol using biogenic gold and silver nanoparticles derived from *Breynia rhamnoides*. *Langmuir* **2011**, *27*, 15268–15274. [CrossRef] [PubMed]
71. Mejía, Y.R.; Bogireddy, N.K.R. Reduction of 4-nitrophenol using green-fabricated metal nanoparticles. *RSC Adv.* **2022**, *12*, 18661–18675. [CrossRef] [PubMed]
72. Asses, N.; Ayed, L.; Hkiri, N.; Hamdi, M. Congo red decolorization and detoxification by *Aspergillus niger*: Removal mechanisms and dye degradation pathway. *BioMed Res. Int.* **2018**, *2018*, 3049686. [CrossRef] [PubMed]
73. Naseem, K.; Farooqi, Z.H.; Begum, R.; Irfan, A. Removal of Congo red dye from aqueous medium by its catalytic reduction using sodium borohydride in the presence of various inorganic nano-catalysts: A review. *J. Clean. Prod.* **2018**, *187*, 296–307. [CrossRef]
74. Ma, T.; Yang, W.; Liu, S.; Zhang, H.; Liang, F. A comparison reduction of 4-nitrophenol by gold nanospheres and gold nanostars. *Catalysts* **2017**, *7*, 38. [CrossRef]
75. Copéret, C.; Estes, D.P.; Larmier, K.; Searles, K. Isolated surface hydrides: Formation, structure, and reactivity. *Chem. Rev.* **2016**, *116*, 8463–8505. [CrossRef] [PubMed]

76. Drew, H.R.; Wing, R.M.; Takano, T.; Broka, C.; Tanaka, S.; Itakura, K.; Dickerson, R.E. Structure of a B-DNA dodecamer: Conformation and dynamics. *Proc. Natl. Acad. Sci. USA* **1981**, *78*, 2179–2183. [CrossRef] [PubMed]
77. Li, J.; Xu, B.; Liu, G.; Chen, G.; Zhang, T.; Zhang, F.; Li, C. Aqueous controllable synthesis of spindle-like palladium nanoparticles and their application for catalytic reduction of 4-nitrophenol. *Prog. Nat. Sci. Mater. Int.* **2016**, *26*, 295–302. [CrossRef]
78. Malik, M.A.; Alshehri, A.A.; Abomuti, M.A.; Danish, E.Y.; Patel, R. Bioengineered *Matricaria recutita* extract-assisted palladium nanoparticles for the Congo red dye degradation and catalytic reduction of 4-nitrophenol to 4-aminophenol. *Toxics* **2021**, *9*, 103. [CrossRef] [PubMed]
79. Ndlovu, L.N.; Malatjie, K.I.; Donga, C.; Mishra, A.K.; Nxumalo, E.N.; Mishra, S.B. Catalytic degradation of methyl orange using beta cyclodextrin modified polyvinylidene fluoride mixed matrix membranes imbedded with in-situ generated palladium nanoparticles. *J. Appl. Polym. Sci.* **2023**, *140*, e53270. [CrossRef]
80. Vilas, V.; Philip, D.; Mathew, J. Facile one-pot synthesis of crystalline palladium nanoparticles with exceptional catalytic and antiradical activities. *Mater. Chem. Phys.* **2016**, *170*, 1–11. [CrossRef]
81. Wang, T.; Su, J.; Jin, X.; Chen, Z.; Megharaj, M.; Naidu, R. Functional clay supported bimetallic nZVI/Pd nanoparticles used for removal of methyl orange from aqueous solution. *J. Hazard. Mater.* **2013**, *262*, 819–825. [CrossRef] [PubMed]
82. Haritha, E.; Roopan, S.M.; Madhavi, G.; Elango, G.; Al-Dhabi, N.A.; Arasu, M.V. Environmental friendly synthesis of palladium nanoparticles and its photocatalytic activity against diazo dye to sustain the natural source. *J. Clust. Sci.* **2017**, *28*, 1225–1236. [CrossRef]
83. Bhat, I.U.H.; Anwar, M.N.K.; Appaturi, J.N. Polymer based palladium nanocatalyst for the degradation of nitrate and Congo red. *J. Polym. Environ.* **2019**, *27*, 1475–1487. [CrossRef]
84. Ismail, S.; Ahmed, W.; Farooq, M.; Rehman, N.U. Plasma-assisted synthesis of gold-silver core-shell nanoparticles and their enhanced catalytic dye degradation and surface enhanced Raman spectroscopy performance. *J. Vac. Sci. Technol. B* **2024**, *42*, 024005. [CrossRef]

Disclaimer/Publisher's Note: The statements, opinions and data contained in all publications are solely those of the individual author(s) and contributor(s) and not of MDPI and/or the editor(s). MDPI and/or the editor(s) disclaim responsibility for any injury to people or property resulting from any ideas, methods, instructions or products referred to in the content.